New Technique for High Resolution Absolute Conductivity Imaging Using Magnetic Resonance-Electrical Impedance Tomography (MR-EIT)

Özlem Birgül [a], B Murat Eyüboğlu [a] and Y Ziya İder [b]

[a]Middle East Technical University, Dept. of Electrical and Electronics Engineering 06531 Ankara, Turkey

[b]Bilkent University, Dept. of Electrical and Electronics Engineering 06533, Ankara, Turkey

ABSTRACT

A novel MR-EIT imaging modality has been developed to reconstruct high-resolution conductivity images with true conductivity value. In this new technique, electrical impedance tomography (EIT) and magnetic resonance imaging (MRI) techniques are simultaneously used. Peripheral voltages are measured using EIT and magnetic flux density measurements are determined using MRI. The image reconstruction algorithm used is an iterative one, based on minimizing the difference between two current density distributions calculated from voltage and magnetic flux density measurements separately. The performance of the proposed method and the suggested reconstruction algorithm are tested on simulated data. A finite element model with 1089 nodes and 2048 triangular elements is used to generate the simulated potential and magnetic field measurements. A 16 electrode opposite drive EIT strategy is adopted. The spatial resolution is space independent and limited by either the finite element size or half the MR resolution. The worst of the two defines the spatial resolution. The rms error in reconstructed conductivity for a concentric inhomogeneity is calculated as 5.35% and this error increases to 13.22% when 10% uniformly distributed random noise is added to potential and magnetic flux density measurements. The performance of the algorithm for more complex models will also be presented.

Keywords: electrical impedance tomography, magnetic resonance imaging, current density imaging

1. INTRODUCTION

Electrical impedance tomography (EIT) is the common name given to imaging modalities used to image the conductivity distribution inside a volume conductor. Accurate conductivity images reconstructed using EIT can be used in applications such as solving bioelectric field problems,[1,2] imaging respiratory function[3] and other applications summarized in.[4]

In conventional EIT technique, current is applied to the volume conductor object either by injection or induction and the peripheral voltage measurements are acquired to find the conductivity distribution inside the object.[5,6] In injected current EIT, electrodes placed at the boundary of the object is used for both excitation and measurement. The number of peripheral voltage measurements are practically limited since the number of electrodes that can be placed on the surface of the object is limited. Moreover, since the conductivity perturbations in the inner parts of the imaging regions does not alter the peripheral voltage measurements as much as the perturbations close to the boundary, the sensitivity of the voltage measurements is not uniformly distributed. Therefore, the reconstructed images have low spatial resolution and space dependent sensitivity.[7]

It is possible to increase the number of independent voltage measurements using induced current EIT techniques.[8,9] In induced EIT, the volume conductor is probed using induced currents created by coils placed around the object and different current distributions are achieved using various coil configurations.[10] Although the number of independent measurements can be increased using this approach, the problem of space dependent resolution still exists. In magnetic induction tomography (MIT) the coils placed around the object are used both for excitation

and data acquisition.[11] An other approach for impedance imaging is the measurement of magnetic flux density generated due to injected currents using magnetometers.[12] Since the measurements can only be done outside the imaging region, the sensitivity of measurements are also less sensitive to conductivity perturbations in the inner regions.

An alternative is the use of magnetic resonance imaging techniques. It has been shown that magnetic flux generated during current injection can be measured using MRI for dc,[13–15] rf,[16] and low frequency ac[17,18] current cases. The magnetic flux density measurements are performed from the inner parts of the object. These flux density measurements are used to calculate the current density distribution inside the object.[13,16,19] For dc currents, the theoretical limit for the spatial resolution of current density is half of the MRI image resolution and data acquisition time is the same as standard spin echo pulse data acquisition scheme.[19] For ac current case, the theoretical limit for spatial resolution is equal to that of the MRI image acquired but practically, due to long data acquisition times for ac currents, practical resolution poor.[20]

Although the images reconstructed using magnetic flux density measurements are of high spatial resolution, they all suffer from the uniqueness problem. In other words, the true (absolute) conductivity distribution can not be reconstructed from magnetic flux measurements only.[21]

Magnetic resonance-electrical impedance tomography (MR-EIT) is a novel imaging technique that reconstructs electrical conductivity distribution combining the conventional magnetic resonance imaging (MRI) and EIT techniques.[22] In this technique, employing the peripheral voltage measurements together with the magnetic flux density, the absolute conductivity images can be reconstructed with high resolution.

In this study, a new MR-EIT technique is proposed. The peripheral voltage measurements from EIT and magnetic flux measurements from (MRI) are simultaneously used. The peripheral voltage measurement are acquired using 16 electrode opposite drive EIT strategy (*set1*). The magnetic flux density is measured using MRI (*set2*). An iterative reconstruction algorithm that minimizes the difference between two current density values calculated using *set1* and *set2* separately is implemented. The proposed method and the suggested reconstruction algorithm are tested using various simulation data. The space dependence of spatial resolution is tested using high contrast point objects. The performance in the presence of noise is also analyzed by adding simulated noise to data. The results imply that it is possible to reconstruct absolute conductivity images with high spatial resolution using the suggested method.

In next sections, first the forward problem of MR-EIT will be defined. Forward problem solution is used in reconstruction procedure with some modifications. It is also used to generate the simulation data. Next, the algorithm suggested for image reconstruction is given. Finally simulation results are presented.

2. FORWARD PROBLEM

Calculation of peripheral voltage values and the flux density distribution for a known conductivity distribution and boundary conditions is defined as the *forward problem*. For the two dimensional problem in Fig. 1, the relation between the conductivity and potential distribution is given by the Poisson's relation as:

$$\nabla \cdot (\sigma \nabla \phi)(x, y) = 0 \qquad\qquad (x, y) \in S \qquad\qquad (1)$$

together with the boundary conditions:

$$\sigma \frac{\partial \phi}{\partial n} = \begin{cases} J & \text{on positive current electrode} \\ -J & \text{on negative current electrode} \\ 0 & \text{elsewhere} \end{cases} , \qquad\qquad (2)$$

where $\sigma(x, y)$ is the electrical conductivity, ϕ is the electrical potential and S is the slice of the object to be imaged.

Analytical solutions for complex conductivity distributions are not available for the Neumann boundary value problem (NBVP) given by Eqs (1) and (2) . In order to solve this NBVP, finite element method (FEM) with a FEM mesh that contains 1089 nodes and 2048 triangular elements is used. The conductivity is assumed to be constant within each element. After calculation of potential distribution, ϕ, the electric field and current density inside the object are calculated using

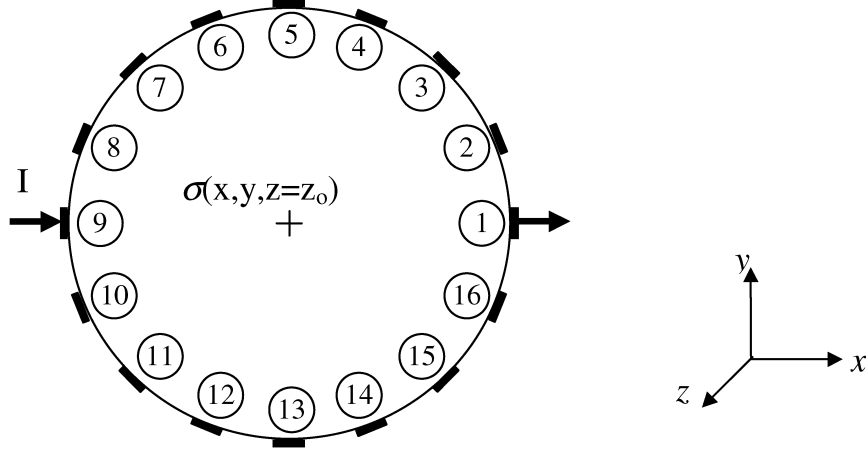$$\vec{E} = -\nabla \phi \qquad\qquad (3)$$

Figure 1. Definitions for 2D object

and

$$\vec{J} = \sigma \vec{E}. \tag{4}$$

Next, the magnetic flux density is calculated using the Biot-Savart Law:

$$\vec{B} = \frac{\mu_0}{4\pi} \int \frac{\vec{J} dS \times \hat{a}_R}{R^2}. \tag{5}$$

3. IMAGE RECONSTRUCTION

Image reconstruction or inverse problem solution is the calculation of inner conductivity distribution using the peripheral voltage measurements, the magnetic flux density measurements and the known boundary conditions. In the following sections, the data acquisition procedures and the image reconstruction algorithm are explained.

3.1. Voltage Measurements

A sixteen-electrode opposite-drive current injection strategy for EIT is adopted. First, an opposite electrode pair is used for excitation and 13 independent voltage measurements are made using the rest of the electrodes. The procedure is repeated for 8 times using different opposite pairs and a total of 104 measurements are acquired.

3.2. Magnetic Flux Density Measurements

Magnetic flux density values can not be measured directly but be extracted from MR images acquired during current injection. The pulse sequence that should be used to find the magnetic flux density distribution is given in Fig. 2. This pulse sequence is a spin echo sequence together with the synchronized bipolar dc current pulse. The MR signal equation recorded for this sequence is

$$S(t) = \int_x \int_y K(x, y) M(x, y) \exp\{j\gamma \left(G_x xt + G_y yt_y + B_z^J T_C\right)\} dx dy. \tag{6}$$

In this expression, $M(x, y)$ is the transverse magnetization distribution, G_x and G_y are the magnetic field gradients in x and y directions, t and t_y are the application times for G_x and G_y gradients, γ is the gyromagnetic constant, B_z^J is the component of the current induced magnetic flux in the direction of the main magnetic field, and T_C is the total current injection time. Note that since the application time for G_x gradient is the time variable t, the total phase accumulated from this gradient changes with time. $K(x, y)$ is the term that includes inhomogeneities in the
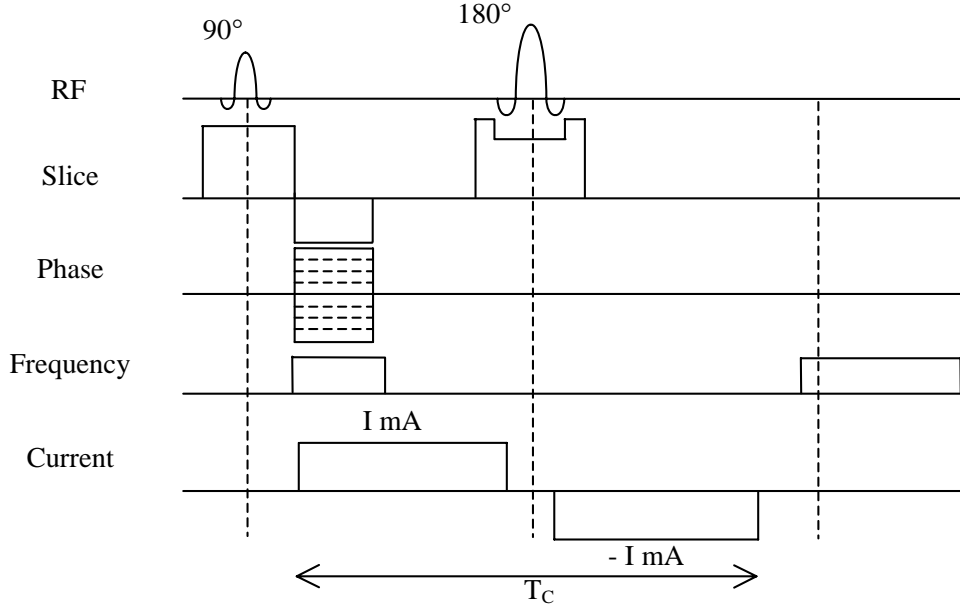
Figure 2. MRI pulse sequence that can be used to find magnetic flux density measurement.[19]

magnetic field and is independent of time and object to be imaged. The complex MR image is obtained from Eq. (6) by taking 2 dimensional inverse Fourier transform as:

$$M_c^J(x,y) = K(x,y)M(x,y)\exp\{j\gamma\left(G_x x t + G_y y t_y + B_z^J T_C\right)\}. \tag{7}$$

The superscript J indicates that the image is acquired during current injection. If there is no current, the MR image will be

$$M_c(x,y) = K(x,y)M(x,y)\exp j\gamma\left(G_x x t + G_y y t_y\right). \tag{8}$$

The phase of the ratio of images in Eqs. (7) and (8) is

$$\Phi_{JN} = \gamma B_z^J(x,y)T_C \tag{9}$$

where Φ_{JN} is the phase normalized with image acquired without current injection. Note that, only the component of the magnetic flux in the direction of the main field of the MR system can be measured at a time. In order to measure all components of the magnetic flux density, the experiment should be repeated three times.

3.3. Iterative Reconstruction Algorithm

A three step iterative reconstruction algorithm is used in the solution of inverse problem. In the first step, the current density inside the object is calculated using

$$\vec{J}_{MR} = \frac{\nabla \times \vec{B}_{MR}}{\mu_0}. \tag{10}$$

MR subscript indicates that the current density is calculated from the magnetic flux density measurements acquired using MRI.

In the next step, the electric field inside the object is found using the peripheral voltage measurements. An initial conductivity distribution is assumed and the electric field is found by solving the boundary value problem defined in Eq. (1) with additional boundary conditions. The peripheral voltage measurements are included in the solution as Dirichlet boundary condition and $\vec{E}_{EIT}$ and $\vec{J}_{EIT}$ are calculated using Eqs. (3) and (4). If the exact conductivity

distribution were known, $\vec{J}_{MR}$ and $\vec{J}_{EIT}$ would be the same. Therefore, the conductivity distribution is selected to minimize the difference between two current density distributions. A residual function is defined as

$$R = \sum_X \int_S \| - \sigma \nabla \phi_{EIT} - \vec{J}_{MR} \| ds \tag{11}$$

where $\| \cdot \|$ is an L_2 norm, X is the number of pairs of electrodes excited and S is the imaging plane. The surface integral is converted into summation over FEM elements as

$$R = \sum_X \sum_j \int_{S_j} \| - \sigma_j \nabla \phi_{EIT} - \vec{J}_{MR} \| ds \tag{12}$$

where j is the element index, σ_j is the conductivity of the jth element and S_j represents the surface of the jth element. R is minimized with respect to each σ_j by setting

$$\frac{\partial R}{\partial \sigma_j} = 0 \tag{13}$$

and the conductivity of the jth element is found as:

$$\sigma_j = -\frac{1}{\mu_0} \frac{\sum_X \int_{S_j} \nabla \phi_{EIT} \cdot \nabla \times \vec{B}_{MR} ds}{\sum_X \int_{S_j} \nabla \phi_{EIT} \cdot \phi_{EIT} ds}. \tag{14}$$

Since a conductivity distribution is assumed in the calculation of $\nabla \phi_{EIT}$, the calculated conductivity will be different from the actual one unless some iteration is done. The conductivity calculated using Eq. (14) is assumed as the new initial conductivity distribution and the procedure is repeated.

4. RESULTS

Several simulations are carried out to test the performance of the suggested MR-EIT iterative reconstruction algorithm. In this section, two error definitions used in the evaluation of the simulation results are given first. Next, the results for spatial resolution are presented. Finally, performance for a more complex phantom that models the human thorax is tested.

In order to generate the simulation noise, first the voltage and the magnetic flux density values corresponding to a uniform conductivity distribution with $0.002 S\ cm^{-1}$ conductivity are calculated. Then, a random noise with uniform distribution that has maximum value equal to 5%, 10%, and 20% of the maximum value of the measurements is generated. Noise sets are generated for voltage measurements and for x,y, and z components of the magnetic flux density separately.

4.1. Error Definitions

Two error values are defined for the reconstructed images. The conductivity error is defined between the actual and reconstructed conductivity values and can be used only with the simulation data where the actual conductivity distribution is known. If σ_{jr} and σ_{jc} are the real and reconstructed conductivity values for the jth element, conductivity error is

$$\varepsilon_\sigma = \sqrt{\frac{1}{N} \sum_{j=1}^{N} \frac{(\sigma_{jr} - \sigma_{jc})^2}{\sigma_{jr}^2}} \times 100\%. \tag{15}$$

where N is the total number of elements in the FEM mesh.

The potential error is defined between the actual peripheral measurements, ϕ_m, and the calculated surface potential values using reconstructed conductivity, ϕ_c, as

$$\varepsilon_\phi = \sum_X \frac{\| \phi_m - \phi_c \|}{\| \phi_m \|} \times 100\% \tag{16}$$

where X is the number of different current injection pairs.

Table 1. Error values in reconstructed images for a concentric point object

	$\varepsilon_\sigma(\%)$	$\varepsilon_\phi(\%)$
noise-free	5.35	8.35
5 % noise	9.63	10.54
10 % noise	13.27	16.72
20 % noise	20.66	30.32

Table 2. Error values in reconstructed images for a eccentric point object

	$\varepsilon_\sigma(\%)$	$\varepsilon_\phi(\%)$
noise-free	5.28	9.57
5 % noise	9.63	11.38
10 % noise	13.22	17.14
20 % noise	20.72	30.69

4.2. Spatial Resolution and Sensitivity

In order to understand the limits of spatial resolution and space dependence of sensitivity, high contrast point object is used. Background and object conductivity values are selected as $0.002S\ cm^{-1}$ and $0.004S\ cm^{-1}$ respectively. The diameter of the object is 1/16 of the whole imaging region diameter. The object is first placed in the middle of the imaging region (*concentric case*) and simulations are carried out for different noise levels. Then, it is shifted to a location that is in the midway between the center and periphery (*eccentric case*). The error values in reconstructed images for noise-free and different noisy cases for the concentric and the eccentric object cases are given in Tables 1 and 2 respectively. 20 iterations are done for all cases. The reconstructed object conductivity values for the noise-free case are $4.34 \times 10^{-3}S\ /cm^{-1}$ and $4.64 \times 10^{-3}S\ /cm^{-1}$ for the concentric and the eccentric objects respectively. The full-width-at-half-maximum (FWHM) values for both the concentric and the eccentric inhomogeneity cases are found to be equal to the size of a pixel.

The conductivity errors are lower than the potential errors for all cases. This is due to the fact that a conductivity errors in elements closer to the boundary causes high potential errors. Therefore, although the total percent error in potential may have high values, corresponding error in reconstructed conductivity is lower.

4.3. Thorax Phantom

In order to understand the performance of the algorithm for complex conductivity distributions, the human thorax phantom in Fig. 3(a) is designed. The conductivity values of different tissues in this model are given in the first column of Table 3. 10 iterations are done for noise-free case and the reconstructed image for this case is given in Fig. 3(b). The average calculated conductivity values are given in the second column of Table 3. The highest error in the reconstructed image is encountered in the regions corresponding to the bone. This is an expected situation since the conductivity of the bone is on the order of 1/100 of the background. Total conductivity and the potential errors are calculated as 9.74% and 28.03% respectively. The high potential error is due to the error made in estimating the conductivity of bone located close to the boundary.

Reconstructed conductivity values when 5% and 10% noise is added to the data are also given in the third and the fourth columns of Table 3. Again, 10 iterations are done for these cases. After the 10th iteration, the error values start to increase and the algorithm diverges. The image reconstructed for 10% noise is given in Fig. 3(c). Note that even in this image, boundaries of different tissues, except for the bone which is close to the boundary, can be easily differentiated. In Fig. 3(d), the image at second iteration for 20% noise is given. The algorithm diverges after the 2nd iteration, but although the errors are quite high, different structures can be differentiated.

5. CONCLUSIONS

In this study, an image reconstruction algorithm that generates absolute conductivity images with high resolution is proposed and tested using simulated data. The FWHM values calculated for small objects placed in different parts

Table 3. Real and reconstructed conductivity values for thorax phantom. All units are $S\ cm^{-1}$

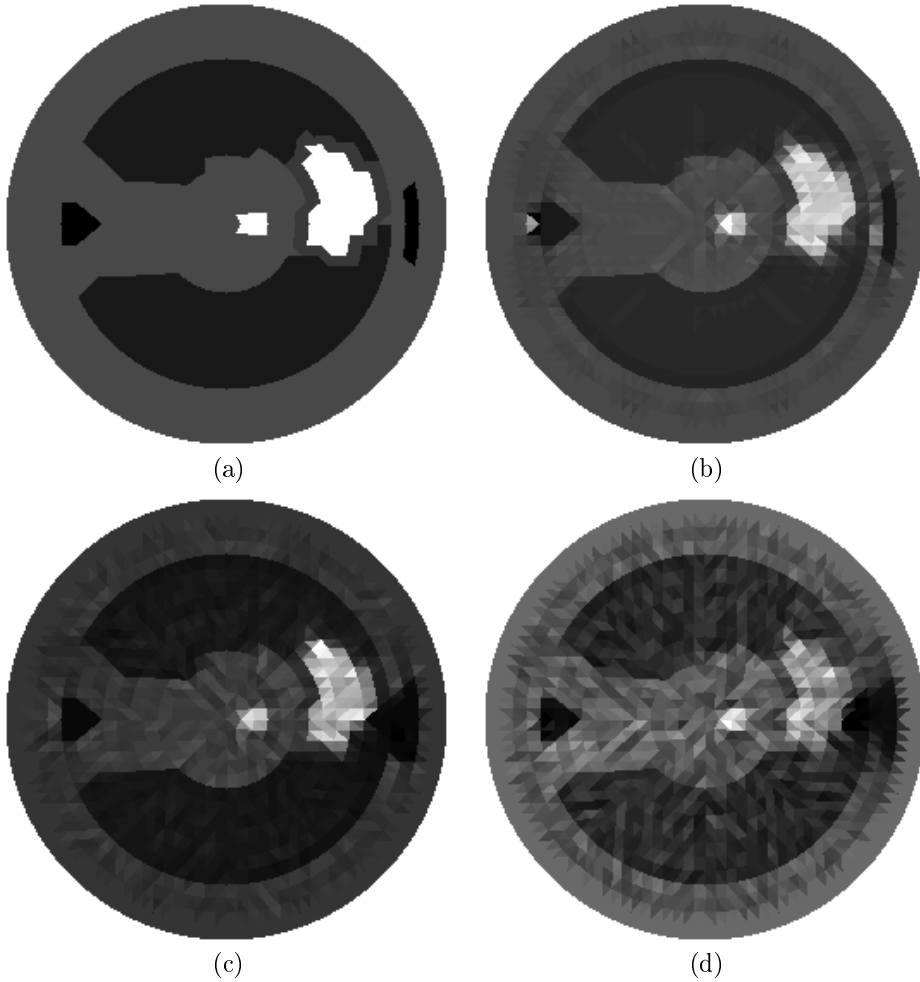| tissue	assigned value	noise-free	5 % noise	10 % noise
blood	6.67×10^{-3}	6.78×10^{-3}	6.86×10^{-3}	6.95×10^{-3}
muscle	1.54×10^{-3}	1.65×10^{-3}	1.54×10^{-3}	1.39×10^{-3}
bone	6.02×10^{-5}	3.17×10^{-5}	2.80×10^{-5}	1.06×10^{-5}
lung	7.69×10^{-4}	7.11×10^{-4}	6.68×10^{-4}	6.15×10^{-4}
background	2.00×10^{-3}	2.90×10^{-3}	2.89×10^{-3}	2.82×10^{-3}

(a)   (b)

(c)   (d)

Figure 3. Original and reconstructed thorax images. (a) Thorax phantom, (b) reconstructed image for 5 %noise, (c) for 10 %noise, (d) for 20 %noise

of the imaging plane show that the sensitivity is independent of the location. For the FEM mesh used, the spatial resolution is limited with the pixel size. If the size of the elements are reduced, the MR image resolution may be the limiting factor for the spatial resolution. The true (absolute) conductivity values can be found with at most $10 - 15\%$ error for the point objects.

The potential error is higher than the conductivity error for all cases. This arises from the fact that small conductivity errors which are close to boundary causes relatively higher potential errors.

For complex conductivity distributions, the method and the suggested algorithm yields images with well defined boundaries. The error in reconstructed conductivity values for lung, blood and muscle regions are below 20% for a simulation noise of 20% and below 12% for a simulation noise of 10%. However, the errors in bone and background conductivity are quite high. The high error in bone conductivity is an expected result since the conductivity of bone is on the order of 1/100 of the background conductivity.

The results imply that the suggested method and algorithm can reconstruct absolute conductivity images with high spatial resolution. Experimental validation and 3D extension are the topics that are being studied in the ongoing work.

ACKNOWLEDGMENTS

REFERENCES

1. S. Gonçalves, J. D. de Munck, R. M. Heethaar, F. H. Lopes da Silva, and B. W. van Dijk, "The applications of electrical impedance tomography to reduce systematic errors in the EEG inverse problem-a simulation study," *Physiol. Meas.* **21**, pp. 379–393, 2000.
2. M. V. van Burik and M. J. Peters, "Estimation of the electric conductivity from scalp measurements: feasibility and application to source localization," *Clin. Neurophysiol.*, **111**, pp. 1514–1521, 2000.
3. I. Frerichs, "Electrical impedance tomography (EIT) in applications related to lung and ventilation: a review of experimental and clinical activities," *Physiol. Meas.* **21**, pp. R1–R21, 2000.
4. J. P. Morucci and B. Rigaud,"Bioelectrical Impedance Techniques in Medicine Part III: Impedance Imaging, Medical Applications," *Critical Reviews in Biomedical Engineering*, pp. 622–677, 1996.
5. K. Boone, D. C. Barber, and B. H. Brown, "Imaging with Electricity: Report of the European Concerted Action on Impedance Tomography," *J. of Medical Engineering and Technology*, **21**, no. 6, pp. 201–232, 1997.
6. B. Rigaud and J. P. Morucci, "Bioelectrical Impedance Techniques in Medicine Part III: Impedance Imaging, General Concepts" *Critical Reviews in Biomedical Engineering*, pp. 467–479, 1996.
7. B. M. Eyüboğlu, B. H. Brown, and D. C. Barber "Limitations to SV Determination from APT Images," *Proc. of 11th Annual International Conference of IEEE EMBS, Seattle USA*, pp. 442–443, 1989.
8. N. G. Gençer, Y. Z. İder, and M. Kuzuoğlu, "Electrical Impedance Tomography Using Induced Currents," *IEEE Trans on BME*, **13**, pp. 338–350, 1994.
9. I. L. Freeston and R. C. Tozer, "Impedance Imaging Using Induced Currents,", *Physiol. Meas.* **16**, Issue SUPPL. 3A, pp. A257–A266, 1995.
10. N. G. Gençer, Y. Z. İder, and S. J. Williamson, "Electrical Impedance Tomography: Achieved with a Multiple Coil System," *IEEE Trans. on BME*, **43**, no. 2, pp. 139–149 1996.
11. A. Korjenevsky, V. Cherepenin, and S. Sapetsky, "Magnetic induction tomography: experimental realization," *Physiol. Meas.* **21**, pp. 89–94, 2000.
12. S. Ahlfors and R. Ilmoniemi, "Magnetic Imaging of Conductivity," *Proc. of 14th Annual International Conference of IEEE EMBS*, , pp. 1717–1718, 1992.
13. G. C. Scott, M. L.G. Joy, R. L. Armstrong, and R. M. Hankelman, "Measurement of Non-Uniform Current Density by Magnetic Resonance," *IEEE Trans. on MI*, **10**, no. 3, pp. 362–374, 1991.
14. G. C. Scott, M. L.G. Joy, R. L. Armstrong, and R. M. Hankelman, "Sensitivity of Magnetic Resonance Current Density Imaging," *J. of Magnetic Resonance*, **97**, pp. 235–254, 1992.
15. B. M. Eyüboğlu, R. Reddy, and J. S. Leigh, "Measurement of Electrical Current Density with Magnetic Resonance Imaging," *IEEE Annual Medical Imaging Conference*, pp. 1472–1473, 1995.

16. G. C. Scott, M. L.G. Joy, R. L. Armstrong, and R. M. Hankelman, "Rotating Frame RF Current Density Imaging," *Magnetic Resonance in Medicine*, **33**, pp. 355–369, 1996.

17. Y. Z. İder, L. T. Müftüler, and Ö. Birgül, "Use of MRI for measuring AC internal currents of EIT: a feasibility study," *Proc. of IXth International Conf. on Electrical Bio-Impedance in conjunction with European Concerted Action on Impedance Tomography* pp. 420–422, 1995.

18. Y. Z. İder and L. T. Müftüler, "Measurement of magnetic field generated by non-uniform AC current density using magnetic resonance imaging," *IEEE Trans. on MI*, **16** no.15 pp. 617–622, 1997

19. B. M. Eyüboğlu, R. Reddy, and J. S. Leigh,"Imaging electrical current density using nuclear magnetic resonance," *Elektrik Turkish J. of Elec. Eng. and Comp. Sci.* **6** no.3 pp. 201–214, 1998.

20. Ö. Birgül and Y. Z. İder, "Electrical impedance tomography using magnetic field generated by internal currents," *Proc. of IEEE EMBS Conf.* cd-rom, 1997.

21. Y. Z. İder and Ö. Birgül, "Use of magnetic field generated by the internal distribution of injected currents for electrical impedance tomography (MR-EIT)," *Elektrik Turkish J. of Elec. Eng. and Comp. Sci.* **6** no.3 pp. 215–225, 1998.

22. Ö. Birgül, B. M. Eyüboğlu, and Y. Z. İder, "Magnetic resonance- conductivity imaging," *Proc. of IEEE EMBS Conf.*, p. 1127, 1999.